Journal of Atmospheric and Solar-Terrestrial Physics 115-116 (2014) 87–94

Contents lists available at ScienceDirect

Journal of Atmospheric and Solar-Terrestrial Physics

journal homepage: www.elsevier.com/locate/jastp

Wavelength dependence of solar irradiance enhancement during X-class flares and its influence on the upper atmosphere

Yanshi Huang [a,*], Arthur D. Richmond [b], Yue Deng [c], Phillip C. Chamberlin [d], Liying Qian [b], Stanley C. Solomon [b], Raymond G. Roble [b], Zuo Xiao [e]

[a] Department of Electrical and Computer Engineering, University of New Mexico, NM, USA
[b] High Altitude Observatory, National Center for Atmospheric Research, Boulder, CO, USA
[c] Department of Physics, University of Texas at Arlington, TX, USA
[d] Solar Physics Laboratory, NASA Goddard Space Flight Center, Greenbelt, MD, USA
[e] Department of Geophysics, Peking University, Beijing, China

ARTICLE INFO

Article history:
Received 26 April 2013
Received in revised form
25 September 2013
Accepted 11 October 2013
Available online 5 November 2013

Keywords:
Solar flare
FISM
TIE-GCM

ABSTRACT

The wavelength dependence of solar irradiance enhancement during flare events is one of the important factors in determining how the Thermosphere–Ionosphere (T–I) system responds to flares. To investigate the wavelength dependence of flare enhancement, the Flare Irradiance Spectral Model (FISM) was run for 61 X-class flares. The absolute and the percentage increases of solar irradiance at flare peaks, compared to pre-flare conditions, have clear wavelength dependences. The 0–14 nm irradiance increases much more (~680% on average) than that in the 14–25 nm waveband (~65% on average), except at 24 nm (~220%). The average percentage increases for the 25–105 nm and 122–190 nm wavebands are ~120% and ~35%, respectively. The influence of 6 different wavebands (0–14 nm, 14–25 nm, 25–105 nm, 105–120 nm, 121.56 nm, and 122–175 nm) on the thermosphere was examined for the October 28th, 2003 flare (X17-class) event by coupling FISM with the National Center for Atmospheric Research (NCAR) Thermosphere–Ionosphere-Electrodynamics General Circulation Model (TIE-GCM) under geomagnetically quiet conditions ($Kp=1$). While the enhancement in the 0–14 nm waveband caused the largest enhancement of the globally integrated solar heating, the impact of solar irradiance enhancement on the thermosphere at 400 km is largest for the 25–105 nm waveband (EUV), which accounts for about 33 K of the total 45 K temperature enhancement, and ~7.4% of the total ~11.5% neutral density enhancement. The effect of 122–175 nm flare radiation on the thermosphere is rather small. The study also illustrates that the high-altitude thermospheric response to the flare radiation at 0–175 nm is almost a linear combination of the responses to the individual wavebands. The upper thermospheric temperature and density enhancements peaked 3–5 h after the maximum flare radiation.

1. Introduction

A solar flare results from a sudden, intense release of magnetic energy in the atmosphere of the Sun, which produces rapid increases in electromagnetic radiation, from gamma rays to radio wavelengths (Einar and Gordon, 1988). Flares are classified as A, B, C, M, or X according to the maximum flux of 0.1–0.8 nm X-rays measured near the Earth (Garcia, 2000). While C-class flares are a common occurrence during years near solar maximum, the frequency of X-class flares during solar maximum is approximately two per month (http://spacemath.gsfc.nasa.gov). There are large spectral variations among flares (Thomson et al., 2004; Tsurutani et al., 2005; Chamberlin et al., 2012). The enhancement of the Extreme Ultraviolet (EUV, ~25 to ~120 nm) spectral irradiance depends on the location of a flare, whereas the flare enhancement of X-ray Ultraviolet (XUV, ~0.1 to ~25 nm) radiation depends only weakly on location (Qian et al., 2010).

Solar EUV photons are the primary energy source of the neutral and ionized constituents of the Thermosphere–Ionosphere (T–I) system (Mitra, 1974; Liu et al., 2011). The extra ionization in the ionosphere caused by flares increases electron density, which influences the absorption and refraction of radio waves propagating through the ionosphere from one station to another (Einar and Gordon, 1988). Also, flares are often associated with Coronal Mass Ejections (CMEs), which may cause significant geomagnetic storms

* Corresponding author. Tel.: +1 7349722340.
E-mail addresses: huangys@unm.edu, yanshi.huang@mavs.uta.edu (Y. Huang), richmond@hao.ucar.edu (A.D. Richmond), yuedeng@uta.edu (Y. Deng), phillip.c.chamberlin@nasa.gov (P.C. Chamberlin), lqian@ucar.edu (L. Qian), stans@ucar.edu (S.C. Solomon), roble@hao.ucar.ed (R.G. Roble), zxiao@pku.eud.cn (Z. Xiao).

1364-6826/$ - see front matter © 2013 Elsevier Ltd. All rights reserved.
http://dx.doi.org/10.1016/j.jastp.2013.10.011

(Munro et al., 1979; Harrison, 1987; Tsurutani et al., 1988; Gonzalez et al., 1994; Michalek, 2009; Bein et al., 2012). Previous studies have shown that the impact of flares on the T–I system varies because flares have different magnitudes, locations on the solar disk, rise rates and decay rates (Tsurutani et al., 2005; Sutton et al., 2006; Qian et al., 2010, 2011; Zhang et al., 2011, 2012). Since XUV dominates ionization in the lower thermosphere (<150 km), and EUV dominates in the upper thermosphere (Qian et al., 2011), the impact of solar flares on the upper atmosphere depends on the solar irradiance enhancement at different wavelengths.

The purpose of this paper is to investigate how different wavebands of solar irradiance are enhanced during flares and how they impact the global thermosphere. The Flare Irradiance Spectral Model (FISM) (Chamberlin et al., 2007, 2008) was employed to estimate the spectra of solar irradiance. The National Center for Atmospheric Research (NCAR) Thermosphere–Ionosphere-Electrodynamics General Circulation Model (TIE-GCM) (Roble et al., 1988; Richmond et al., 1992) driven by the FISM was used to simulate the thermospheric responses to flares.

2. Model description

2.1. Flare irradiance spectral model (FISM)

FISM is an empirical model of the solar irradiance spectrum from 0.1 to 190 nm at 1 nm resolution and on 1-minute time cadence. The high temporal resolution of FISM makes it possible to study the variations due to solar flares. This model is based on the data provided by the Solar Extreme ultraviolet Experiment (SEE) (Woods et al., 2005) on the Thermosphere Ionosphere Mesosphere Energetics and Dynamics (TIMED) satellite, and the SOLar STellar Irradiance Comparison Experiment (SOLSTICE) (Rottman, 2000) on the Solar Radiation and Climate Experiment (SORCE).

FISM estimates the daily component of irradiance, including the variations from the solar cycle and solar rotation of active regions (Chamberlin et al., 2007). The flare component of FISM includes both the impulsive and gradual phase variations, and is based on a reference set of 39 large flares from 2002 to 2005 measured by SEE and SORCE (Chamberlin et al., 2008). This reference set of measurements is fit to a flare proxy to determine the coefficients. The Geostationary Operational Environmental Satellites (GOES) 0.1–0.8 nm fluxes are used as the flare proxy to empirically model the flare variation for FISM, because of its high temporal resolution and reliable data since 1970 with few data gaps, as well as plans for continued future measurements. A linear relation is found between the irradiance of GOES 0.1–0.8 nm and the irradiance for the X-rays at wavelengths less than 14 nm, while a power law relation with exponent of 0.647 is found between the irradiance of GOES 0.1–0.8 nm and the irradiance for EUV at wavelengths larger than 14 nm (Chamberlin et al., 2008).

Due to large variations during flares for different wavelengths, and due to limited measurements, the FISM flare uncertainty has a wavelength dependence that varies from 10% to above 100%. However, compared to models with only daily outputs, FISM improves the estimation of solar flares significantly. More flare data can help reduce the FISM flare uncertainties. The newly available and more accurate data from the Extreme ultraviolet Variability Experiment (EVE) on the Solar Dynamics Observatory (SDO) (Woods et al., 2010, 2011) will add the additional variable of temporal delays in some of the EUV emissions during the gradual phase of flares (Chamberlin et al., 2012).

2.2. NCAR TIE-GCM

The NCAR TIE-GCM is a first-principles, three-dimensional, nonlinear representation of the coupled thermosphere and ionosphere system. It solves the momentum, energy and continuity equations for neutral and ion species in pressure coordinates (Roble et al., 1988), with a self-consistent calculation of ionospheric wind dynamo effects (Richmond et al., 1992). The external forcings of TIE-GCM are mainly the solar irradiance, magnetospheric energy, and tidal perturbations at the lower boundary of the model. Magnetospheric energy inputs include auroral particle precipitation and high-latitude ion convection. In this study, the Heelis potential model (Heelis et al., 1982) was used to specify the high-latitude electric field while the auroral particle precipitation is as described by Roble and Ridley (1987). The latest version (v1.94) of the TIE-GCM was run with a $5^\circ \times 5^\circ \times$ half scale height resolution (longitude $\times$ latitude $\times$ vertical).

Solar irradiance spectra estimated by the FISM were used as solar input to the TIE-GCM in our study. The spectral range required by the TIE-GCM is 0.05–175 nm, so the part of FISM spectra at wavelengths greater than 175 nm is not included. The low-resolution binning scheme developed by Solomon and Qian (2005) is utilized to separate the FISM spectrum into 37 bins for the solar EUV energy deposition calculation. The spectrum between 0.05–105 nm is divided into 22 non-uniform bins according to the changes of cross sections and photon energy within a bin. The part of spectra with wavelengths longer than 105 nm is divided evenly into 5-nm bins except for the *Lyman* $-\alpha$ line (121.56 nm) (Qian, 2007).

The heating due to solar irradiance from 0.05 to 105 nm is calculated through integrating heating over the first 22 bins as shown by Wang (1998) in Eq. (2.8), which depends on the solar flux at different wavelengths, the ionization cross sections of N_2, O_2, and O, and the column number densities of N_2, O_2, and O. The contribution of the Schumann–Runge continuum (105–175 nm) is integrated over the remaining 15 bins. The photodissociation by radiation in the Schumann–Runge continuum is the primary direct dissociation process for O_2 in the thermosphere. The excess energy from O_2 dissociation goes directly into heating, which is about 6.6% of the absorbed Schumann–Runge radiation (Schunk and Nagy, 2009). The quenching process of $O(^1D)$ resulted in the O_2 dissociation also contributes to the neutral heating. The neutral gas heating by the Schumann–Runge bands is specified by the empirical formula in Strobel (1978), with a heating efficiency of about 0.3.

3. Results and discussion

3.1. Solar irradiance enhancements from the FISM for X-class flares

A flare is classified as A, B, C, M or X according to the peak flux of 0.1–0.8 nm irradiance near the Earth. Within each class, a linear scale from 1.0 to 9.9 is used to specify the magnitude of a flare, except for X-class flares, the class number can exceed 9.9. The biggest flare in the National Oceanic and Atmospheric Administration (NOAA) records is an X28 flare that occurred on November 4, 2003. The November 4, 2003, flare saturated GOES X-ray sensor (XRS), and its magnitude was initially estimated as X28 through extrapolating the GOES curve (http://www.swpc.noaa.gov). Thomson et al. (2004) argued that the magnitude of this X28 flare should be as large as X45 5 based on the measurements of ionospheric VLF (Very Low Frequency) radio phase change.

Fig. 1 depicts the FISM outputs for the X17 flare on October 28th, 2003 (day of year 301). The top panel shows the temporal variation of total solar flux integrated over 0–190 nm wavelengths, which started to increase at 11:00 UT and reached a maximum flux of 100 mW/m^2 at around 11:07 UT. Solar spectra before the flare and at the flare peak are shown in the middle panel. The black line is for the pre-flare time which is marked with a triangle in the top panel, whereas the red line is for the time at the flare peak which

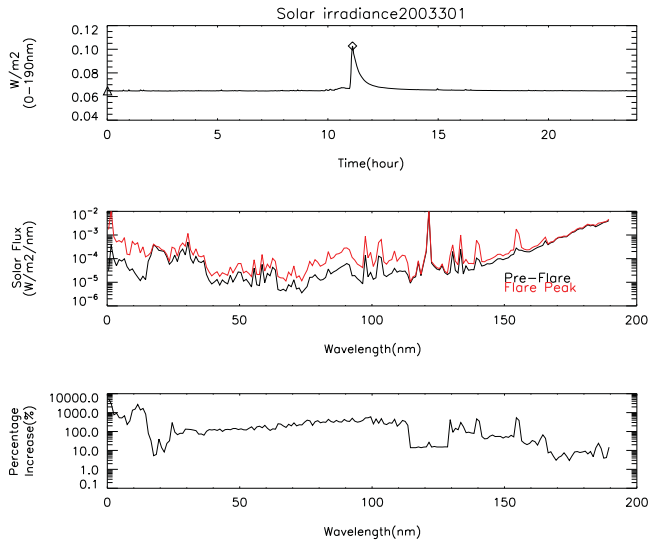

Fig. 1. FISM solar irradiance results for the X17 flare on October 28th, 2003 (day of year 301). Top: time variation of total solar irradiance integrated over the wavelengths from 0 to 190 nm. The flare reached a maximum flux of 0.1 W/m^2 at around 11:07 UT. Middle: solar spectra before the flare at the moment denoted by the triangle in the top panel (black) and at the flare peak denoted by the diamond (red). Bottom: percentage increase of solar irradiance comparing the peak and pre-flare conditions. (For interpretation of the references to color in this figure caption, the reader is referred to the web version of this article.)

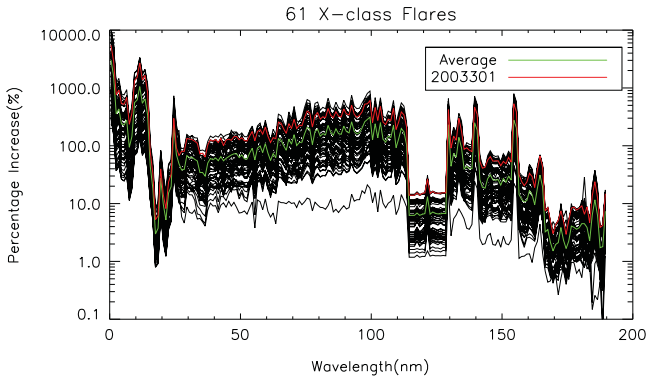

Fig. 2. FISM solar irradiance results for the percentage increases comparing the peak and pre-flare conditions for the 61 X-class flares that occurred between year 1989 and 2012. The red line denotes the October 28th, 2003, flare event, and the green line is the average of the 61 X-class flares. The low enhancement at 15–25 nm is a result of the depletion of source ions, whereas the low enhancement at 115–129 nm, except for the 121.56 nm bin, is rather instrumental. The lower envelope longer than 25 nm is for the X1.5 flare that occurred on April 21, 2002. (For interpretation of the references to color in this figure caption, the reader is referred to the web version of this article.)

is marked with a diamond in the top panel. The clear peak at about 121.56 nm before the flare is the emission line of hydrogen Lyman-α, which will be discussed in more details later. The flux enhancement varied with wavelength, as illustrated in the bottom panel, which shows the percentage increase of solar flux at the flare peak compared to the pre-flare condition. The solar irradiance increased the most in the 0–14 nm range, about 1500% on average, whereas it only increased ~100% in the 14–25 nm range, except at 24 nm (~300%). The average enhancements of irradiance in the 25–105 nm and 122–190 nm wavebands are about 230% and 70% for this flare, respectively. The solar irradiance increase modeled by the FISM is for the brief, initial enhancement during the impulsive phase of this flare.

In order to have a better understanding of the wavelength dependence of irradiance enhancement of X-class flares, we examined the spectra of solar irradiance percentage increase during 61 X-class flares between 1989 and 2012 using the FISM. These flares ranged from X1.0 to X28, and mostly occurred in the maximum and descending phases of solar cycles. The 20 X-class flares occurred during 2002–2005 among these 61 flare events along with another 19 M-class flares are the 39 large flares that are used as the basis of FISM (Chamberlin et al., 2008). Fig. 2 shows the percentage increase of the 61 X-class flares. The red line denotes the October 28th, 2003 flare event, and the green line is the average of the 61 X-class flares. The 0–14 nm irradiance increases much more (~680% on average) than that for the 14–25 nm waveband (~65% on average), except for the peak at around 24 nm (~220%). The average percentage increases for the 25–105 nm and 122–190 nm wavebands are ~120% and ~35%, respectively. There is a relatively small enhancement in the 14–25 nm wavelength range, which contains many strong solar emission lines, such as Fe IX. When a flare occurs, these emissions do not increase very much, and sometimes even decrease (Woods et al., 2011). This is because most of these emissions are formed in the solar corona at the approximate temperature of the corona, around 1–2 million K. When the source ions are heated to much higher temperatures, Fe IX quickly ionizes to higher states, depleting the source ion population for Fe IX emissions, so that there is a relatively small enhancement in the 15–25 nm wavelength range. On the other hand, the low enhancement in the 115–129 nm range, excluding the 1 nm hydrogen Lyman-α bin at 121.56 nm, is rather instrumental. In the TIMED/SEE instrument, which FISM is based on, an aluminum filter had to be put in place to block 99% of the Lyman-α emission line at 121.56 nm so that it would not saturate the detector and still be enough to be measured (Eparvier et al., 2001). This filter blocks the entire 115–129 nm band, which is then assumed to vary in the same manner as the Lyman-α emission that is measured by SEE.

In this study, the XUV/EUV spectrum is divided into six wavebands according to the penetration depth in the atmosphere and the irradiance enhancement during flares: 0–14 nm and 14–25 nm wavebands for XUV, 25–105 nm and 105–120 nm for EUV, the Lyman-α line (121.56 nm), and the 122–175 nm waveband for far ultraviolet (FUV) irradiance. We will investigate how these wavebands contribute to thermosphere responses to the X17-class flare that occurred on October 28th, 2003, one of the most severe flares in the last solar cycle.

3.2. Temporal variation of thermosphere response at 400 km

To evaluate the influence on the thermosphere of the 0–14 nm radiation for the October 28th, 2003 flare, the TIE-GCM was run holding all radiation constant at the pre-flare level except for that in the 0–14 nm band, which was varied as prescribed by the FISM. The difference between this run and a base TIE-GCM run with constant radiation in all wavebands was then evaluated. The influence of solar irradiance enhancement for the other wavebands was calculated in the same way. To minimize geomagnetic influences, all the simulations are under geomagnetically quiet conditions ($Kp=1$). In this study, the globally integrated or averaged values were analyzed to focus on large-scale responses.

The temporal variations of solar irradiance flux in the 0–14 nm, 25–105 nm and 122–175 nm wavebands were selected and emphasized, since they contain most of the solar irradiance enhancement (Fig. 3). The solar flux variations for different wavebands calculated by the FISM are depicted in the first row. The solar flux in the 0–14 nm waveband is quite small before the flare (~ 1 mW/m^2), as compared with that in the 122–175 nm waveband (~ 12 mW/m^2), but it increased the most (~ 20 mW/m^2) at the flare peak. It is also noticed that the peak time of solar flux varies. Although the total flux

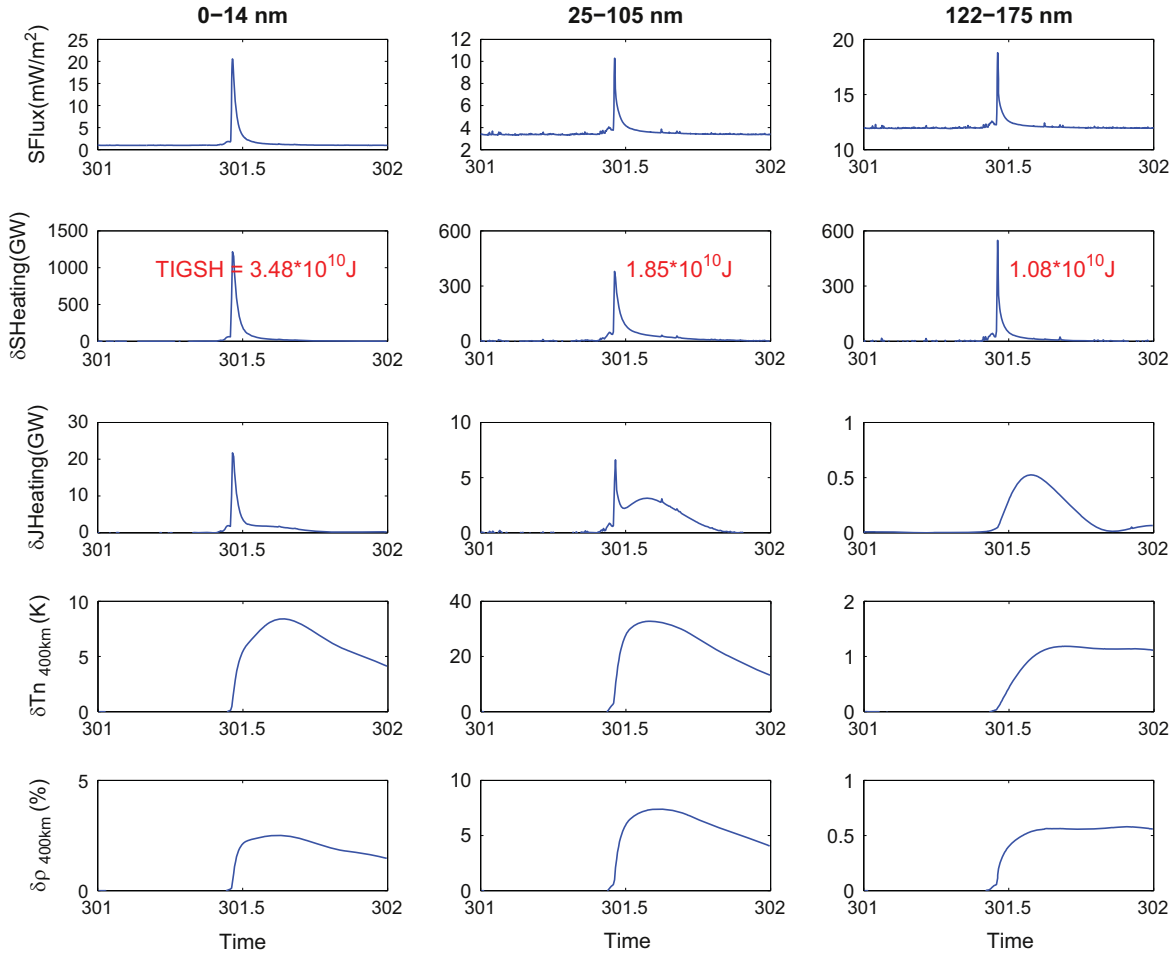

Fig. 3. Time variations of different wavebands for DOY 301, first column for 0–14 nm, second column for 25–105 nm and third column for 122–175 nm. Top row: solar irradiance calculated by the FISM. Second row: perturbation of global heating due to solar irradiance. The time integration (one day) of global solar heating (TIGSH) deposited is labeled in red. Third row: perturbation of globally integrated Joule heating. Fourth row: Globally averaged perturbation of temperature at 400 km. Bottom row: Globally averaged perturbation of neutral density at 400 km. (For interpretation of the references to color in this figure caption, the reader is referred to the web version of this article.)

integrated from 0 to 190 nm peaked at 11:07 UT, the fluxes for 105–120 nm and 122–190 nm peaked earlier at 11:05 UT, those for 25–105 nm and 121 nm peaked at 11:06 UT, the flux for 14–25 nm peaked at 11:07 UT, and that for 0–14 nm peaked at 11:10UT. Therefore, except for the Lyman-α emission line, basically the peak time decreases with the increasing wavelength. The second row shows the enhancement of globally integrated solar heating in the upper atmosphere during the flare, which was calculated by taking the difference between the flare and non-flare runs for each waveband. The peak solar heating for the 0–14 nm waveband is the largest ($\sim$1216 GW), which is more than three times as large as the peak for the 25–105 nm waveband ($\sim$379 GW). The time integration (one day) of global solar heating (TIGSH) for the 25–105 nm waveband (1.85×10^{10} J) is only half of that for the 0–14 nm waveband ($\sim3.48\times10^{10}$ J) but is larger than that for the 122–175 nm waveband ($\sim1.08\times10^{10}$ J). In the third row, Joule heating enhancement due to increased Pedersen conductivity shows quite different responses in time and magnitude for different wavebands. There is a rather rapid and large enhancement of Joule heating responding to the solar flare irradiance for the 0–14 nm waveband. However, for 122–175 nm, the peak of the Joule heating enhancement has an obvious delay with respect to the flare peak. The response for 25–105 nm is a combination of the patterns for the 0–14 nm and the 122–175 nm wavebands. The radiation at 122–175 nm impacts the thermosphere through dissociation and heating, but not ionization, and is absorbed by O_2, which has significant densities only in the lower thermosphere. Therefore, it affects the Pedersen conductivity indirectly through affecting the neutral temperature and density in the lower thermosphere, which in turn affect the ion density and ion-neutral collision frequency. Due to the fact that the neutral temperature and density changes persist longer than the ionization enhancements, the associated changes of Pedersen conductivity and Joule heating also persisted hours after the flare. The global Joule heating increased, but the magnitude was quite small compared with the global heating due to the solar irradiance. Joule heating in these results was rather small because the imposed high-latitude electric field was relatively small.

The fourth and bottom rows of Fig. 3 depict the thermospheric temperature and density perturbations at 400 km, which is close to altitudes of some Low-Earth Orbiting (LEO) satellites, such as the Challenging Minisatellite Payload (CHAMP). The total temperature and neutral density perturbations at 400 km were $\sim$45 K and $\sim$11.5%, respectively. The thermospheric perturbations at 400 km due to solar irradiance enhancement at 25–105 nm ($\sim$33 K increase of temperature; $\sim$7.4% increase of neutral density) are much larger than at 0–14 nm ($\sim$8 K increase of temperature; $\sim$2.5% increase of neutral density). The enhancement of the 122–175 nm waveband resulted in little effect on the high-altitude thermospheric responses. Most of the irradiance in 122–175 nm is absorbed by O_2 in the lower thermosphere. Some of the heat

Table 1
Heating efficiency of solar irradiance at different wavelengths to thermosphere at 400 km for the X17 flare event on October 28th, 2003 (day of year 301).

	0–14 nm	25–105 nm	122–175 nm
δ SH peak (GW)	1216	379	548
TIGSH (J)	3.48e10	1.85e10	1.08e10
δ Tn peak (K)	8.4	32.8	1.2
$\delta\rho$Peak	2.50%	7.39%	0.58%
δ Tn/δ SH (K/GW)	0.0069	0.0865	0.0022
δ Tn/TIGSH (K/J)	2.41e − 10	17.73e − 10	1.09e − 10
$\delta\rho/\delta$SH (%/GW)	0.0021	0.0200	0.0011
$\delta\rho$/TIGSH (%/J)	0.7e − 10	4.0e − 10	0.5e − 10

deposited in the lower thermosphere conducts up to the upper thermosphere and produces small but long-lasting thermospheric perturbations. On the other hand, the 0–14 nm irradiance is absorbed by O and N_2 as well as O_2. Therefore , it has a larger fraction absorbed in the upper thermosphere compared to the Schumann–Runge continuum (Torr et al., 1979; Roble and Emery, 1983). As the high-altitude atmosphere conducts heat downward over time, the upper thermosphere cools down.

Although the largest heating enhancement comes from solar irradiance in the 0–14 nm wavelength range, most of the thermospheric perturbations at 400 km are due to the 25–105 nm waveband (Table 1). The heating efficiency, which is defined as temperature (density) perturbations divided by the peak solar heating, is an order larger for the 25–105 nm waveband than those for the other two wavebands. Therefore, the solar irradiance in the 25–105 nm wavelength range influences the thermosphere at 400 km most effectively. The maximum high-altitude thermospheric responses occurred 3 ~ 5 h later than the flare peak.

Fig. 4 compares the full simulation including all the variations in the 0–175 nm wavelength range with the summation of perturbations due to the six individual wavebands (0–14 nm, 14–25 nm, 25–105 nm, 105–120 nm, 121.56 nm, and 122–175 nm). The black lines represent the globally averaged perturbations of (a) solar heating deposited into the thermosphere, (b) neutral temperature and (c) density at 400 km due to the whole flare spectrum from 0 to 175 nm, while the red lines represent the summations of perturbations at 400 km due to the six separate bands. The black lines and red lines are very close to each other, which illustrates the nearly linear response of the thermosphere to different wavebands of solar irradiance at 400 km. Therefore, the high-altitude thermospheric response to the 0–175 nm flare radiation is almost a linear combination of the responses to individual wavebands. This suggests a possibility to predict the variations of temperature and neutral density at LEO due to flares using the solar irradiance measurements at different wavebands. For future flares, measurements covering the different wavebands of solar irradiance can give estimations of the thermospheric responses separately, and then the total response is predicted as a linear combination of them.

3.3. Altitudinal distribution of the thermospheric disturbance

The results for the 0–14 nm and 25–105 nm wavebands are further discussed in this section since they have the most significant influence on the thermosphere. Fig. 5(a) depicts the altitudinal distributions of heat perturbations due to solar irradiance enhancement in different wavebands at the flare peak. The largest perturbations of heating per unit mass occur above 150 km, which is dominated by the 25–105 nm waveband, while the heating below 150 km is dominated by the irradiance of 0–14 nm. The solar heating rate per unit mass peaks in the upper thermosphere around 300 km at high solar activity conditions, and it

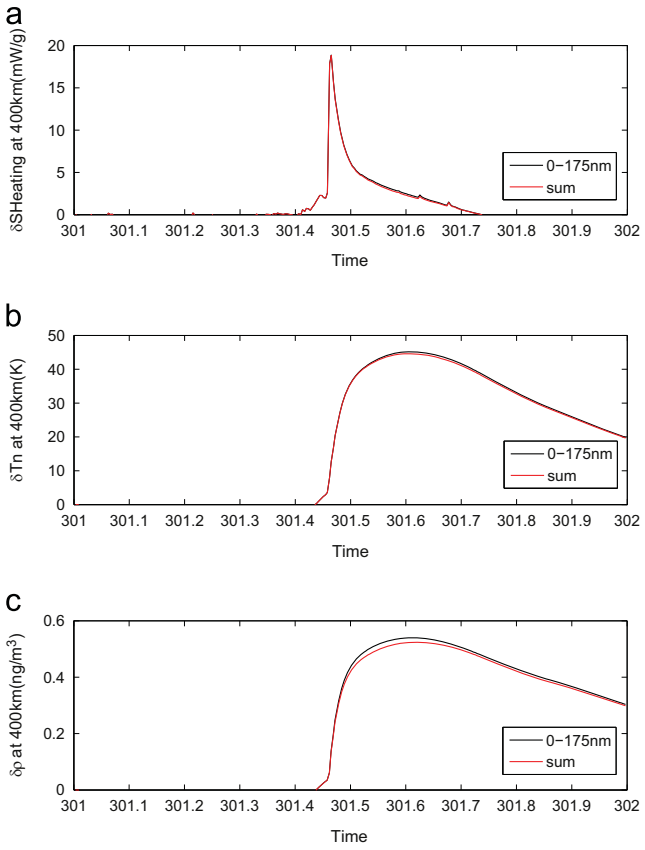

Fig. 4. Comparison between the full simulation that includes the flare enhancements of all wavebands, and the summation of perturbations due to the 6 individual bands (0–14 nm, 14–25 nm, 25–105 nm, 105–120 nm, 121.56 nm, and 122–175 nm). The black lines show the variations using the full 0–175 nm FISM solar spectra, while the red lines represent the sum of variations due to the FISM spectra in the separate wavebands. (a) Globally averaged solar heating perturbation at 400 km. (b) Globally averaged temperature perturbation at 400 km. (c) Globally averaged neutral density perturbation at 400 km. (For interpretation of the references to color in this figure caption, the reader is referred to the web version of this article.)

is dominated by the heating process of neutral–neutral and ion-neutral chemical reactions (Roble et al., 1987). The heating perturbation resulted in similar temperature response, as shown in Fig. 5(b). The temperature perturbation below ~150 km is larger for the solar heating in the 0–14 nm waveband, while for the upper thermosphere above 150 km, the perturbation is dominated by the heating at 25–105 nm. Consequently, the neutral density perturbation around 400 km is dominated by the solar heating in the 25–105 nm waveband as illustrated in Fig. 5(c). Therefore, the solar irradiance at 25–105 nm is significant for high altitude heating at the flare peak, while the irradiance at 0–14 nm plays a dominant role below 150 km.

The temporal and altitudinal responses of the thermosphere to solar flare irradiance varied significantly with wavelength. Fig. 6 shows the temporal variations of the altitudinal distributions for different wavebands: the first column for the 0–14 nm waveband, the second column for 25–105 nm and the third column for the full waveband from 0 to 175 nm. As shown in the first row, the largest percentage increase of heating due to solar irradiance in the 0–14 nm waveband is below 150 km, while that for 25–105 nm is above 150 km. The total heating due to solar irradiance for the full waveband (0–175 nm) increased up to 140% below ~150 km. The second and third rows show the corresponding perturbations of temperature and neutral density, respectively. The maximum temperature perturbation for 0–175 nm was about 47 K at high altitudes, with ~9 K contributed by the 0–14 nm waveband and ~34 K by the 25–105 nm waveband.

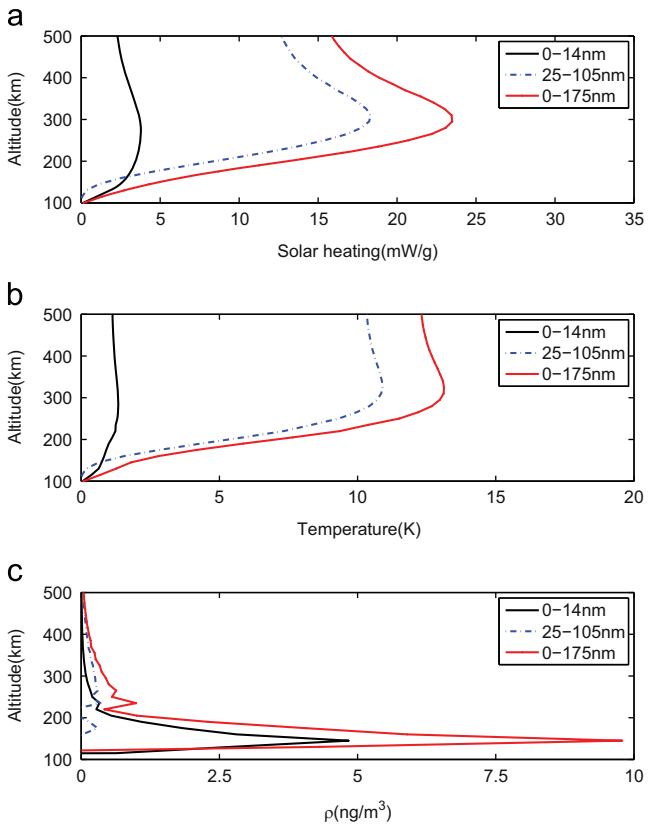

Fig. 5. Altitudinal distribution of TIE-GCM simulation results at the flare peak due to solar irradiance enhancement in different wavelength ranges. (a) Globally averaged heating perturbation. (b) Globally averaged temperature perturbation. (c) Globally averaged neutral density perturbation. The density perturbations below 145 km can sometimes be negative, and only positive values are plotted.

Similarly, the maximum neutral density enhancement due to the 0–175 nm waveband was around 18.8%, with ~3.7% contribution from 0-14 nm and ~12.9% from 25–105 nm. Apparently, the solar irradiance at 25–105 nm plays a dominant role in impacting the upper atmosphere. It can be explained by the fact that the upper thermospheric response is much stronger to the heating in the upper thermosphere than to the heating in the lower thermosphere (Deng et al., 2011; Huang et al., 2012).

The white lines in the middle and bottom rows of Fig. 6 represent the moments of the largest temperature and density enhancements at different altitudes. The moments of maximum temperature perturbations denoted by the white line (second row) correspond well to the solar heating at different altitudes (first row). For the 0–14 nm waveband, the maximum temperature enhancement at about 150 km occurs quickly corresponding to the maximum heating at the same altitude. Then the heat conducts upward and downward, gradually heating the surrounding thermosphere. For the 25–105 nm waveband, since most of the heat is deposited above 150 km, the heat conduction is mainly downward. Therefore it takes longer time to heat the lower thermosphere. The peak upper thermospheric perturbation had 3–5 h time delay compared to the flare peak. The large-scale gravity waves, which are generated by thermospheric heating and expansion on the dayside, transport energy from dayside to nightside. Pawlowski and Ridley (2008) investigated the global thermospheric response to the October 28, 2003, flare and found that the gravity wave propagates at the speed of local sound speed plus the neutral wind velocity. The global mean sound speed at 400 km is around 900 m/s and the average neutral wind speed is around 200 m/s. Therefore, with a total speed of 1100 m/s, it takes about 5 h for the wave to travel from dayside to nightside.

For this study, in order to focus on the solar flare influence on the upper atmosphere and minimize the geomagnetic effect, we did a non-realistic simulation with constant $Kp=1$. Therefore, the

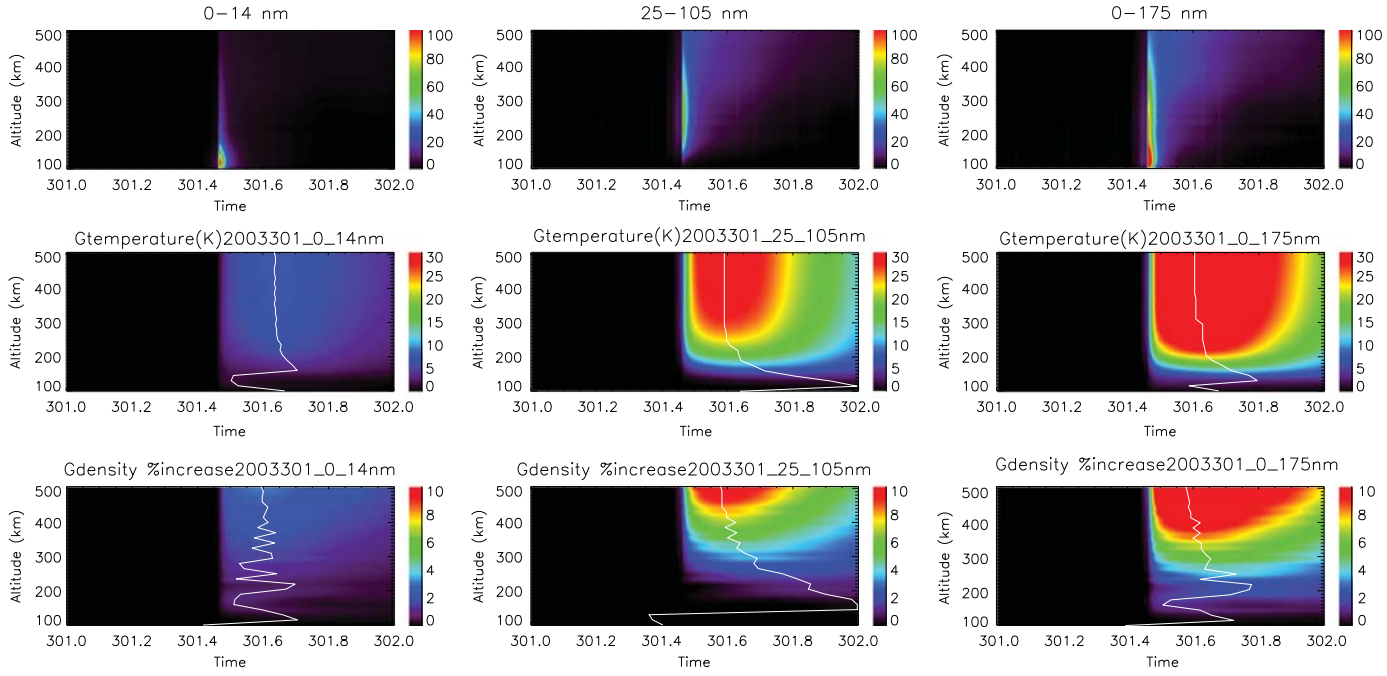

Fig. 6. Temporal variations of the altitudinal distribution of TIE-GCM simulation results due to solar irradiance enhancement in the 0–14 nm, 25–105 nm and 0–175 nm wavelength ranges. First row: globally averaged percentage increase of solar heating that deposited in the thermosphere. Second row: globally averaged temperature enhancement. Third row: globally averaged percentage increase of neutral density. The white lines represent the moments of the largest temperature and density enhancements at different altitudes. The density enhancement below 145 km can sometimes be negative.

comparison between neutral density from our TIE-GCM runs and the observations from CHAllenging Minisatellite Payload (CHAMP)/GRACE Gravity Recovery And Climate Experiment (GRACE) could not be used to validate our model results.

4. Conclusions

The responses of the thermosphere to solar flares vary in magnitude and duration, since flares have different energy deposition heights, magnitudes and durations for different wavebands. The wavelength dependence of the solar flare enhancement is one of the important factors in determining how the terrestrial atmosphere responds to flares. The FISM spectra show that for the 61 X-class solar flares that occurred between 1989 and 2012, the solar irradiance enhancement at the flare peak relative to the pre-flare condition has a clear wavelength dependence. The 0–14 nm irradiance increases much more (~680% on average) than that for the 14–25 nm waveband (~65% on average), except at around 24 nm (~220%). The average percentage increases for the 25–105 nm and 122–190 nm wavebands are ~120% and ~35%, respectively.

The thermospheric response to six different wavebands of solar irradiance for the X17-class solar flare on October 28th, 2003, was investigated through coupling the FISM to the TIE-GCM as solar input. The globally integrated solar heating and the one-day integration of it are largest in the 0–14 nm waveband. However, the impact of solar irradiance enhancement on the upper thermosphere is largest for the 25–105 nm waveband (EUV). At ~400 km, it accounts for about 33 K of the total 45 K temperature enhancement, and ~7.4% of the total ~11.5% neutral density enhancement. For this particular simulation, the maximum temperature perturbation is ~47 K (34 K due to EUV irradiance), and the maximum neutral density perturbation is ~18.8% (12.9% due to EUV irradiance) at higher altitude than 400 km. The effect of 122–175 nm (FUV) irradiance is small. The high-altitude temperature and neutral density enhancements maximize 3 – 5 h after the flare peak. The comparison between a full simulation including all the variation at 0–175 nm wavelengths and the summation of perturbations due to the six individual wavebands indicates that at 400 km, there is a nearly linear response of the thermosphere to different wavebands of solar irradiance. It suggests a possibility to predict the variations of temperature and neutral density at LEO due to flares using the solar irradiance measurements at different wavebands.

Acknowledgments

We acknowledge the LASP Interactive Solar Irradiance Data center for FISM data. This research was supported by the National Science Foundation through grant ATM0955629 and by the Air Force Office of Scientific Research through grant 1210429. Part of this work was conducted while Y.H. and Y.D. were visitors in the Advanced Study Program at the National Center for Atmospheric Research (NCAR). NCAR is sponsored by the National Science Foundation.

References

Bein, B.M., Berkebile-Stoiser, S., Veronig, A.M., Temmer, M., Vršnak, B., 2012. Impulsive acceleration of Coronal Mass Ejections. II. Relation to soft X-ray flares and filament eruptions. Astrophys. J. 755 (1), 44, http://dx.doi.org/10.1088/0004-637X/755/1/44.

Chamberlin, P.C., Woods, T.N., Eparvier, F.G., 2007. Flare irradiance spectral model (FISM): daily component algorithms and results. Space Weather 5, S07005, http://dx.doi.org/10.1029/2007SW000316.

Chamberlin, P.C., Woods, T.N., Eparvier, F.G., 2008. Flare irradiance spectral model (FISM): flare component algorithms and results. Space Weather 6, S05001, http://dx.doi.org/10.1029/2007SW000372.

Chamberlin, P., Milligan, R., Woods, T., 2012. Thermal evolution and radiative output of solar flares observed by the EUV variability experiment (EVE). Sol. Phys. 279 (1), 23–42.

Deng, Y., Fuller-Rowell, T.J., Akmaev, R.A., Ridley, A.J., 2011. Impact of the altitudinal Joule heating distribution on the thermosphere. J. Geophys. Res. 116, A05313, http://dx.doi.org/10.1029/2010JA016019.

Einar, Tandberg-Hanssen, Gordon Emslie, A., 1988. The Physics of Solar Flares. Cambridge Astrophysics Series. Cambridge University Press, Cambridge-New York-New Rochelle-Melbourne-Sydney.

Eparvier, F.G., Woods, T.N., Ucker, G.J., Woodraska, D.L., 2001. TIMED solar EUV experiment: preflight calibration results for the EUV grating spectrograph. SPIE Proc. 4498, 91–100, http://dx.doi.org/10.1117/12.450049.

Garcia, H.A., 2000. Thermal spatial analysis of medium and large solar flares: 1976 to 1996. Astrophys. J. 127 (Suppl.), 189–210, http://dx.doi.org/10.1086/313312.

Gonzalez, W.D., Joselyn, J.A., Kamide, Y., Kroehl, H.W., Rostoker, G., Tsurutani, B.T., Vasyliunas, V.M., 1994. What is a geomagnetic storm? J. Geophys. Res. 99 (A4), 5771–5792, http://dx.doi.org/10.1029/93JA02867.

Harrison, R.A., 1987. Solar Soft X-ray Pulsations. A&A 182, 337.

Heelis, R., Lowell, J., Spiro, R., 1982. A model of the high-latitude ionospheric convection pattern. J. Geophys. Res. 87 (A8), 6339–6345.

Huang, Y., Richmond, A.D., Deng, Y., Roble, R., 2012. Height distribution of Joule heating and its influence on the thermosphere. J. Geophys. Res. 117, A08334, http://dx.doi.org/10.1029/2012JA017885.

Liu, L., Wan, W., Chen, Y., Le, H., 2011. Solar activity effects of the ionosphere: a brief review. Chin. Sci. Bull. 56 (12), 1202–1211, http://dx.doi.org/10.1007/s11434-010-4226-9.

Michalek, G., 2009. Two types of flare-associated coronal mass ejections. Astron. Astrophys. 494, 263.

Mitra, A.P., 1974. Ionospheric Effects of Solar Flares. Springer, New York.

Munro, R.H., Gosling, J.T., Hildner, E., MacQueen, R.M., Poland, A.I., Ross, C.L., 1979. The association of coronal mass ejection transients with other forms of solar activity. Sol. Phys. 61, 201.

Pawlowski, D.J., Ridley, A.J., 2008. Modeling the thermospheric response to solar flares. J. Geophys. Res. 113, A10309, http://dx.doi.org/10.1029/2008JA013182.

Qian, L., 2007. Modeling Thermospheric Neutral Density. Pennsylvania State University, ISBN: 0549272712, 9780549272717.

Qian, L., Burns, A.G., Chamberlin, P.C., Solomon, S.C., 2010. Flare location on the solar disk: modeling the thermosphere and ionosphere response. J. Geophys. Res. 115, A09311, http://dx.doi.org/10.1029/2009JA015225.

Qian, L., Burns, A.G., Chamberlin, P.C., Solomon, S.C., 2011. Variability of thermosphere and ionosphere responses to solar flares. J. Geophys. Res. 116, A10309, http://dx.doi.org/10.1029/2011JA016777.

Richmond, A.D., Ridley, E.C., Roble, R.G., 1992. A thermosphere/ionosphere general circulation model with coupled electrodynamics. Geophys. Res. Lett. 19, 601–604.

Roble, R.G., Emery, B.A., 1983. On the global mean temperature of the thermosphere. Planet. Space Sci. 31, 597–614.

Roble, R.G., Ridley, E.C., 1987. An auroral model for the NCAR thermospheric general circulation model. Ann. Geophys. 5a (6), 369.

Roble, R.G., Ridley, E.C., Dickinson, R.E., 1987. On the global mean structure of the thermosphere. J. Geophys. Res. 92 (A8), 8745–8758, http://dx.doi.org/10.1029/JA092iA08p08745.

Roble, R.G., Ridley, E.C., Richmond, A.D., Dickinson, R.E., 1988. A coupled thermosphere/ionosphere general circulation model. Geophys. Res. Lett. 15, 1325–1328.

Rottman, G., 2000. Solar UV irradiance measurements: the UARS and EOS SOLSTICE. Phys. Chem. Earth Part C: Sol. Terr. Planet. Sci. 25 (5–6), 401–404, ISSN: 1464-1917, 10.1016/S1464-1917(00)00042-8.

Schunk, R.W., Nagy, A.F., 2009. Ionosphere, Second Edition Cambridge University Press.

Solomon, S.C., Qian, L., 2005. Solar extreme-ultraviolet irradiance for general circulation models. J. Geophys. Res. 110, A10306, http://dx.doi.org/10.1029/2005JA011160.

Strobel, D.F., 1978. Parameterization of the atmospheric heating rate from 15 to 120 km due to O_2 and O_3 absorption of solar radiation. J. Geophys. Res. 83, 6225–6237.

Sutton, E.K., Forbes, J.M., Nerem, R.S., Woods, T.N., 2006. Neutral density response to the solar flares of October and November, 2003. Geophys. Res. Lett. 33, L22101, http://dx.doi.org/10.1029/2006GL027737.

Thomson, N.R., Rodger, C.J., Dowden, R.L., 2004. Ionosphere gives the size of greatest solar flare. Geophys. Res. Lett. 31, L06803, http://dx.doi.org/10.1029/2003GL019345.

Torr, M.R., Torr, D.G., Ong, R.A., Hinteregger, H.E., 1979. Ionization frequencies for major thermospheric constituents as a function of solar cycle 21. Geophys. Res. Lett. 6, 771–774, http://dx.doi.org/10.1029/GL006i010p00771.

Tsurutani, B.T., Gonzalez, W.D., Tang, F., Akasofu, S.-I., Smith, E.J., 1988. Origin of interplanetary southward magnetic fields responsible for major magnetic storms near solar maximum (1978–1979). J. Geophys. Res. 93, 8519–8531.

Tsurutani, B.T., et al., 2005. The October 28, 2003 extreme EUV solar flare and resultant extreme ionospheric effects: comparison to other Halloween events and the Bastille Day event. Geophys. Res. Lett. 32, L03S09, http://dx.doi.org/10.1029/2004GL021475.

Wang, W., 1998. A Thermosphere–Ionosphere Nested Grid (TING) Model. University of Michigan, ISBN: 9780599084896.

Woods, T.N., Eparvier, F.G., Bailey, S.M., Chamberlin, P.C., Lean, J., Rottman, G.J., Solomon, S.C., Tobiska, W.K., Woodraska, D.L., 2005. Solar EUV experiment

(SEE): mission overview and first results. J. Geophys. Res. 110, A01312, http://dx.doi.org/10.1029/2004JA010765.

Woods, T.N., et al., 2010. Extreme ultraviolet variability experiment (EVE) on the solar dynamics observatory (SDO): overview of science objectives, instrument design, data products, and model developments. Sol. Phys. , http://dx.doi.org/10.1007/s11207-009-9487-6.

Woods, T.N., Hock, R., Eparvier, F., Jones, A.R., Chamberlin, P.C., Klimchuk, J.A., Didkovsky, L., Judge, D., Mariska, J., Warren, H., Schrijver, C.J., Webb, D.F., Bailey, S., Tobiska, W.K., 2011. New solar extreme-ultraviolet irradiance observations during flares. Astrophys. J. 739, 59, http://dx.doi.org/10.1088/0004-637X/739/2/59.

Zhang, D.H., Mo, X.H., Cai, L., Zhang, W., Feng, M., Hao, Y.Q., Xiao, Z., 2011. Impact factor for the ionospheric total electron content response to solar flare irradiation. J. Geophys. Res. 116, A04311, http://dx.doi.org/10.1029/2010JA016089.

Zhang, D.H., Cai, L., Ercha, A., Hao, Y.Q., Xiao, Z., 2012. Statistical studies on the excess peak flux in soft X-rays and EUV bands from solar flares. Sol. Phys. 280, 183–196.